

Topological Hall effect induced by chiral fluctuations in a kagome lattice

Kyle W. Fruhling^{1*}, Alenna Streeter^{1*}, Sougata Mardanya²,
Xiaoping Wang³, Priya Baral⁴, Oksana Zaharko⁴,
Igor I. Mazin⁵, Sugata Chowdhury², William D. Ratcliff^{6,7}, Fazel Tafti^{1*}

¹Department of Physics, Boston College, Chestnut Hill, MA 02467, USA

²Department of Physics and Astrophysics, Howard University, Washington, DC 20059, USA

³Neutron Scattering Division, Oak Ridge National Laboratory, Oak Ridge, TN 37831, USA

⁴Laboratory for Neutron Scattering and Imaging (LNS), Paul Scherrer Institut, PSI,
Villigen, CH-5232, Switzerland

⁵Department of Physics and Astronomy and Quantum Science and Engineering Center,
George Mason University, Fairfax, VA 22030, USA

⁶NIST Center for Neutron Research, National Institute of Standards and Technology,
Gaithersburg, ME 20899-6100, USA

⁷Department of Physics and Department of Materials Science and Engineering,
University of Maryland, College Park, Maryland 20742, USA

*fazel.tafti@bc.edu

One Sentence Summary: Chiral fluctuations at the boundary between antiferromagnetic and ferrimagnetic phases produce a topological Hall effect in the kagome magnet ErMn_6Sn_6 .

Topological Hall effect (THE) is a hallmark of scalar spin chirality, which is found in static skyrmion lattices. Recent theoretical works have shown that scalar spin chirality could also emerge dynamically from thermal spin fluctuations. Evidence of such a mechanism was found in the kagome magnet YMn_6Sn_6 where fluctuations arise from frustrated exchange interactions between Mn kagome layers. In YMn_6Sn_6 , the rare-earth ion Y^{3+} is non-magnetic.

*These authors contributed equally to this work.

When it is replaced by a magnetic ion (Gd^{3+} – Ho^{3+}), the intrinsically antiferromagnetic Mn-Mn interlayer coupling is overwhelmed by the indirect ferromagnetic Mn-*R*-Mn one, relieving frustration. This generates interesting anomalous Hall conductivity, but not THE. Here we show that Er lies in an intermediate regime where direct and indirect interactions closely compete, so that ErMn_6Sn_6 can switch from one regime to the other by temperature, i.e., from a collinear ferrimagnetic ground state to a spiral antiferromagnet at 78 K. The AFM phase forms a dome in the temperature-field phase diagram. Close to the boundary of this dome, we find a sizable fluctuations-driven THE, thus underscoring the universality of this mechanism for generating non-zero scalar spin chirality.

Introduction

The unique geometry of the 2D kagome lattice leads to appreciable frustration in the nearest neighbor magnetic or electronic tight-binding models. While numerous materials with antiferromagnetic (AFM) kagome planes, usually correlated insulators, have been investigated for spin-liquid behavior (1), another class of interest is stacked ferromagnetic kagome layers, which retains the peculiarity of the original kagome model in terms of electronic structure, but not magnetic frustration (2). The electronic structure of such materials is described by a frustrated hopping model, which was originally restricted to *s*-orbitals only (3) but later extended to *d*-orbitals in compounds with hexagonal symmetry (4). Since many of these materials are magnetically ordered above room temperature and easily manipulated by doping, they provide a fascinating playground for topology and magnetism to interact on a kagome lattice and produce exotic behaviors in momentum space, such as flat bands and Dirac crossings (5–7).

One such family of compounds, dubbed “166”, has attracted particular attention. The general formula is RT_6M_6 , where *R* is a rare-earth, *T* is a 3d transition-metal, usually Mn, and

M is a metalloid of the group 13 or 14, most commonly Sn. In all these compounds, the Mn layers are metallic and inherently ferromagnetic (FM); however, the coupling between layers and the anisotropy of the ordered state depend on the rare-earth atom between the layers (8–10). For example, TbMn_6Sn_6 has a strong Tb-Mn coupling and shows an out-of-plane ferrimagnetic (FIM) order, which leads to a sizable anomalous Hall effect (AHE) (11–14). The non-magnetic rare-earths (Y and Sc) have no R -Mn coupling and favor a spiral antiferromagnetic (AFM) coupling between Mn layers, which leads to a sizable topological Hall effect (THE) (15–17). In this paper, we discuss the peculiar case of ErMn_6Sn_6 , a relatively less studied member of the 166 family (18), which falls in a regime between the FIM TbMn_6Sn_6 and spiral AFM YMn_6Sn_6 .

As we will show here, the peculiarity of ErMn_6Sn_6 lies in the strength of the Er-Mn coupling, which is non-zero unlike Y-Mn, but much weaker than Tb-Mn, so the net sign of the Mn-Mn coupling can be reversibly switched by reducing the ordered Er moment through thermal fluctuations. This leads to a change of magnetic state from FIM at low temperatures (similar to TbMn_6Sn_6) to spiral AFM at high temperatures (similar to YMn_6Sn_6). Using field-dependent magnetization and neutron diffraction data, we show that the spiral AFM state occupies a dome in the H - T phase diagram. We also show that the field-induced transition between these two states involves an intermediate regime of fluctuating Mn moments. By performing detailed magneto-transport measurements, we reveal a sizable THE in this fluctuating regime, i.e., at the boundary between the spiral AFM phase (where ErMn_6Sn_6 is analogous to YMn_6Sn_6) and FIM phase (where it is analogous to TbMn_6Sn_6). The magnitude of THE increases with increasing temperature as expected from the fluctuation-driven mechanism.

Results

Magnetization

ErMn_6Sn_6 has a high-temperature AFM transition marked by a peak at $T_N=346(3)$ K in Fig. 1A and a low-temperature FIM order marked by a step in the in-plane susceptibility at $T_C=78(8)$ K.

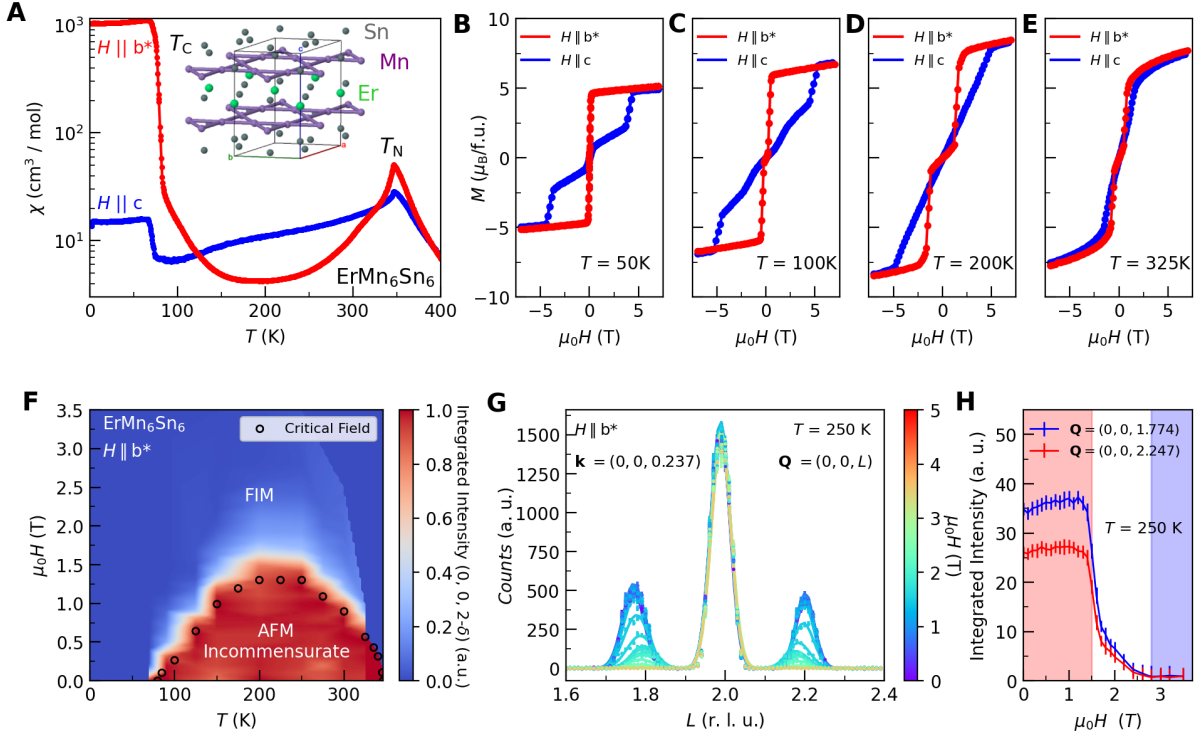


Figure 1: Magnetic Phase Diagram. (A) Magnetic susceptibility of ErMn_6Sn_6 as a function of temperature measured in both in-plane and out-of-plane field directions and plotted on a semilog plot. (B-E) Magnetization as a function of field at several temperatures. (F) Magnetic phase diagram constructed from the in-plane magnetization data (black circles) and neutron diffraction data (color map). The color map represents normalized integrated intensity under incommensurate AFM Bragg peaks. (G) Neutron diffraction \mathbf{Q} scan in the (00L) direction showing a structural Bragg peak at the center and two satellite magnetic peaks. The satellites indicate incommensurate AFM order at $\mathbf{Q} = (0, 0, 2 \pm \mathbf{k})$ with $\mathbf{k} = 0.237$. (H) Field dependence of the integrated intensity under the satellite peaks in panel (G) reveal three regimes at 250 K. Error bars in this paper represent one standard deviation.

The AFM ordering has little anisotropy but the FIM order has a marked easy-plane character, as seen in Fig. 1A. The evolution of anisotropy with temperature is demonstrated in the magnetization curves of Figs. 1B-E. At low temperatures, the out-of-plane magnetization ($H \parallel c$) saturates at a much higher field than in-plane magnetization ($H \parallel b^*$, where b^* is the direction orthogonal to a). However, this anisotropy becomes less pronounced as temperature is increased from $T_C = 78$ K to $T_N = 346$ K.

Using the magnetization curves in Figs. 1B-E and the supplementary Fig. S1, we construct

the magnetic phase diagram of ErMn_6Sn_6 for $H\parallel b^*$ and $H\parallel c$, respectively, in Fig. 1F and the supplementary Fig. S2. Focusing on the red curves ($H\parallel b^*$) in Figs. 1B-E, the $M(H)$ curve at 50 K (Fig. 1B) shows a rapid saturation of the magnetic moment characteristic of FIM ordering. However, the $M(H)$ curves at higher temperatures (Figs. 1C-E) show a linear regime at low fields characteristic of AFM ordering, followed by a saturation due to a field-induced transition from the AFM to FIM order. The black data points in Fig. 1F trace this field-induced transition between AFM (linear regime) and FIM (saturated regime) orders, revealing an AFM dome in the phase diagram.

Neutron Diffraction

We used single crystal neutron diffraction to characterize the FIM and AFM structures, and study their evolution with magnetic field in the phase diagram of Fig. 1F. It is instructive to start with the AFM dome at the center of the phase diagram. Fig. 1G shows diffraction patterns at several fields along the $\mathbf{Q} = (0, 0, L)$ direction at 250 K. The central peak at $\mathbf{Q} = (0, 0, 2)$ is a structural Bragg peak and the two satellites at $\mathbf{Q} = (0, 0, 2 \pm \mathbf{k})$, with $\mathbf{k} = 0.237$, are incommensurate AFM Bragg peaks. Previous diffraction studies at zero field (19) show that upon decreasing temperature, these satellite peaks move closer to the structural $(0, 0, 2)$ peak and merge with it at $T_C=78$ K, the temperature of the AFM to FIM transition at $H = 0$.

We studied the evolution of satellite peaks not only with temperature but also with in-plane magnetic field ($H\parallel b^*$). As seen in Fig. 1G, the incommensurate satellite peaks are suppressed with increasing in-plane field and vanished at 3 T. By tracing the integrated intensity under these satellite peaks as a function of field at 250 K, we reveal three regimes in Fig. 1H shaded with red, white, and blue colors. In the low-field region ($H < 1.5$ T, red), we find a nearly unchanged magnetic intensity under the satellites peaks in the incommensurate AFM phase. In the high-field region ($H > 2.8$ T, blue), the satellite peaks are completely suppressed and the system is in the field-induced FIM phase. In the intermediate region ($1.5 < H < 2.8$ T, white), the satellite peaks are gradually being suppressed. By repeating this analysis at different

temperatures (supplementary Figs. S3 and S4), we constructed the phase diagram of Fig. 1F where the color scale corresponds to the integrated intensity under the satellite peaks at different temperatures. The red region is the incommensurate AFM phase where the satellite peaks are sizable. The blue region is the FIM phase where satellite peaks have vanished. The white region is the intermediate phase where the satellite peaks are being suppressed with field.

A refinement of the neutron diffraction data in the FIM phase yields the collinear in-plane magnetic structure shown in Fig. 2A. Details of the magnetic refinements are presented in the supplemental Figs. S5 and S6 and Tables S1 to S4. The Er and Mn magnetic moments are oppositely oriented with the respective magnitudes of $8.0 \mu_B$ and $2.3 \mu_B$. This structure is consistent with the zero-field ground state of ErMn_6Sn_6 reported in a prior work (19).

The refinement analysis in the AFM phase at 200 K with an incommensurate k -vector (0, 0, 0.1959) produces a spiral order made of Mn-Er-Mn sandwich layers which rotate by 70.4° with respect to each other. The magnetic unit cell is approximately five times the structural unit cell (Fig. 2B). Within a single Mn-Er-Mn sandwich layer, the Mn moments from the top and bottom Mn layers form an angle ϕ and their net magnetization is canceled by the oppositely oriented Er moments. This is the same double spiral order which has been found in YMn_6Sn_6 , now with a moment on the rare-earth site in ErMn_6Sn_6 (15). As seen in Fig. 1H, the transition between the spiral AFM phase and FIM phase is not abrupt; it involves an intermediate regime of fluctuating Mn moments. In the phase diagram of Fig. 1F, this fluctuating regime appears as a pale region between the red (spiral AFM) and blue (FIM) regions. Our magneto-transport measurements, presented below, reveal a sizable THE in this fluctuating regime.

Topological Hall Effect

The known mechanism of THE is due to the static scalar spin chirality (SSC) in non-coplanar magnetic structures, for example, in a skyrmion lattice (20–22). Recently, a dynamical mechanism for the THE has been proposed where spiral fluctuations, complementing an existing static spiral, generate a finite SSC and thus a THE (16, 23, 24). In the 166 compounds, this

mechanism is operative only at finite temperatures, and only in a magnetic phase that is a transverse conical spiral (TCS) propagating along the c -axis. A TCS naturally forms in a material where the zero-field state is a helical spiral and an external magnetic field \mathbf{H} is applied in the ab -plane, a condition that is realized at the AFM phase boundary in ErMn_6Sn_6 (Fig. 1F). A TCS state by itself has zero SSC, but adding another spiral propagating in the direction perpendicular to both c and \mathbf{H} generates a finite SSC. A simple thermodynamic calculation (16) shows that such thermal excitations give a THE that is proportional to the applied field, temperature, and $M_c^2 = M_s^2 - M^2$, which is the projection of the Mn moment onto the c direction,

$$\rho^T = \kappa M_c^2 T H \quad (1)$$

In a prior study of YMn_6Sn_6 with non-magnetic Y^{3+} ions (16), the variable M_c was readily available because Mn was the only magnetic species, and the measured saturation magnetization was a good estimate of M_s , while the field-dependent magnetization was M . Then, the prefactor κ in Eq. 1 would be a constant. In ErMn_6Sn_6 , however, Er^{3+} ions carry a large and strongly temperature-dependent magnetization which prevents us from using Eq. 1 directly, even though it can be used separately at each individual temperature. In other words, κ becomes temperature dependent in ErMn_6Sn_6 . For simplicity, we first present a more conventional method of extracting the THE and leave the implications of Eq. 1 to the Discussions.

We extract the THE from the total Hall signal as shown in Fig. 2C, by subtracting the ordinary ($\rho^O \propto H$) and anomalous ($\rho^A \propto M$) Hall effects from the total signal (ρ^H) to arrive at the topological Hall effect (ρ^T) assuming $\rho^H = R_0 H + 4\pi R_s M + \rho^T$. In the high field FIM state, this assumption holds well and this equation simplifies to $\rho^H = R_0 H + 4\pi R_s M$. Then following the procedure in Ref. (16), we can determine the high field anomalous and ordinary Hall effects by plotting ρ^H/M as a function of H/M and extracting the slope R_0 and intercept $4\pi R_s$. The typical treatment would assume these are both constant; however, the electronic structure and hence R_0 may be different in different magnetic phases. It also assumes that the anomalous Hall effect remains proportional to the magnetization which is not

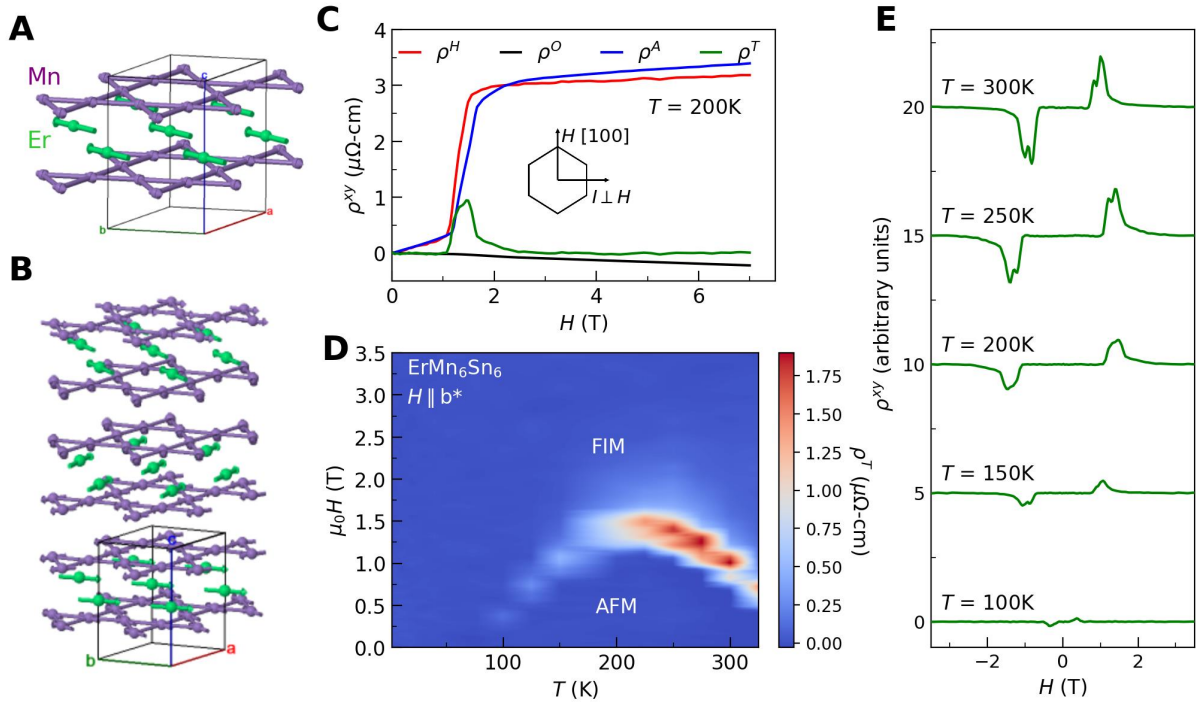


Figure 2: **Topological Hall Effect.** (A) Magnetic unit cell of ErMn_6Sn_6 in the FIM ground state. Arrows in the Mn kagome layer (purple) and Er triangular layer (green) correspond to their respective magnetic moments. Sn atoms are not shown for simplicity. (B) Supercell rendering of the incommensurate helical AFM order. A more detailed view is presented in the supplementary Fig. S6. (C) Topological Hall effect (ρ^T) is extracted by subtracting the ordinary (ρ^O) and anomalous (ρ^A) Hall effects from the total Hall effect (ρ^H). (D) A second version of the phase diagram (Fig. 1F) with a color map that corresponds to the intensity of the THE. (E) Representative $\rho^T(H)$ curves at different temperatures.

a fair assumption for spiral magnets. In the treatment we follow we determine the ordinary Hall effect at low field as $\rho^O = \rho^H - 4\pi R_s M$, and then interpolate a cubic spline for ρ^O between the AFM and FIM states. The sum of the anomalous and ordinary Hall components is then assumed to vary smoothly between phases. Thus the sum can be used to determine ρ^T even if the individual components are not accurately separated in the AFM state. ρ^T is then given by $\rho^T = \rho^H - R_0 H - 4\pi R_s M$. The black, blue, and green lines in Fig. 2C show the ordinary, anomalous, and topological components of the total Hall signal. We repeated this analysis at different temperatures and made a color map of THE (ρ^T) in Fig. 2D. Our Hall data at different temperatures are presented in the supplementary Fig. S7.

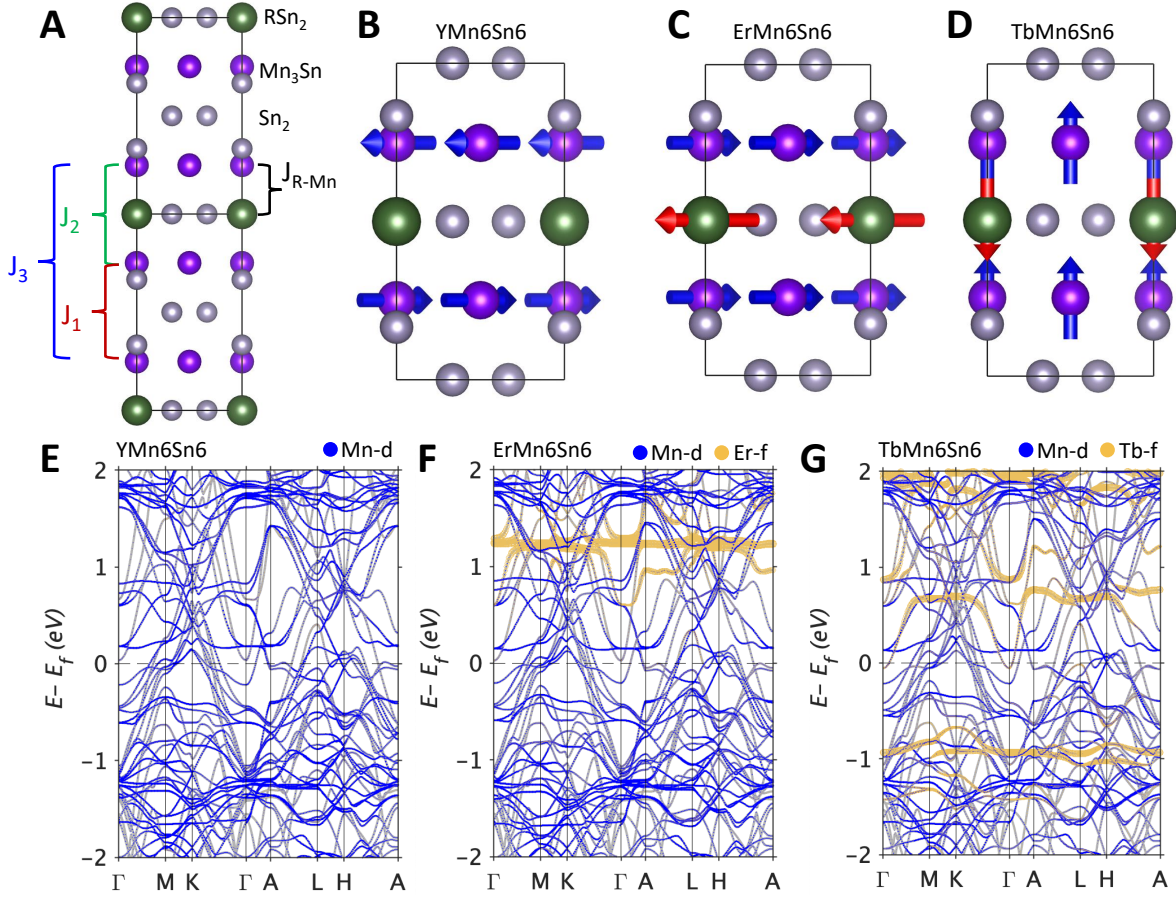


Figure 3: **Magnetic Interactions and Electronic Structure.** (A) Magnetic interactions in the RMn_6Sn_6 system. The ground state magnetic configuration for (B) YMn_6Sn_6 , (C) ErMn_6Sn_6 , and (D) TbMn_6Sn_6 . (E)-(G) The orbital projected electronic structure with spin-orbit coupling along the high symmetry path of the Brillouin zone in YMn_6Sn_6 , ErMn_6Sn_6 , and TbMn_6Sn_6 . The rare-earth f-states are highlighted in orange color.

First-Principles Calculations

To understand the TCS magnetic phase and the emerging THE in ErMn_6Sn_6 , we compare it to its sister compounds YMn_6Sn_6 and TbMn_6Sn_6 . All three compounds share the same configuration of Mn_3Sn Kagome layers sandwiched between two inequivalent Sn_2 and RSn_2 (R =Rare-earth) layers as shown in Fig. 3A. Previous studies (4, 14) have shown that the competition between the magnetic anisotropy of the rare-earth elements and Mn dictates the magnetic phase of these compounds. YMn_6Sn_6 and TbMn_6Sn_6 lie at two extreme ends of this picture. In YMn_6Sn_6 , where the rare-earth element is nonmagnetic, the magnetic anisotropy is fixed by the

easy-plane anisotropy of the Mn layer. In this case, the spiral ground state is well understood by a three-parameter Heisenberg model, consisting of a ferromagnetic J_1 (across the Sn_2 layer), antiferromagnetic J_2 (across the $R\text{Sn}_2$ layer), and a ferromagnetic J_3 (Fig. 3A). Replacing Y with the magnetic atom Tb changes the magnetic anisotropy of the system into a strong easy axis. Additionally, the interaction J_2 between Mn layers across the $R\text{Sn}_2$ layer becomes significantly larger in TbMn_6Sn_6 than in YMn_6Sn_6 . Therefore, the strong coupling from magnetic rare-earth enforces a collinear magnetic state with out-of-plane moments for TbMn_6Sn_6 .

ErMn_6Sn_6 lies in an intermediate regime between the Y and Tb compounds. A comparison between the electronic structure of the three compounds is presented in Figs. 3E-G. In these calculations, the strong correlation effects of the f and d electrons are included by considering an effective onsite Hubbard potential ($U_{\text{eff}} = U - J$) (25, 26). We use $U_{\text{eff}}^{\text{Er}} = 8$ eV, $U_{\text{eff}}^{\text{Tb}} = 7$ eV, following the recommendation of Ref. (27), and $U_{\text{eff}}^{\text{Mn}} = 0.5$ eV. Close to the Fermi level (E_{F}), the electronic structures of the Y and Er compounds look nearly identical. This is because the Er- f states lie well above the E_{F} (1.3 eV) and do not have much influence on the bands near the Fermi level. In contrast, the Tb- f states come closer to the E_{F} and enhance the Tb-Mn interaction. Therefore, the R -Mn exchange coupling is expected to be smaller in ErMn_6Sn_6 than in TbMn_6Sn_6 .

To verify this conjecture, we calculated the exchange coupling constants and found that $J_{\text{Tb-Mn}}$ is at least four times larger than $J_{\text{Er-Mn}}$ (140 meV vs. 32 meV). Given that the direct Mn-Mn exchange coupling J_2 is AFM (and only weakly dependent on the rare earth) but the indirect coupling is FM (Fig. 3A), the net interaction appears antiferro- or ferromagnetic, and the ground state, correspondingly, spiral or ferrimagnetic, depending on which component dominates. In the case of ErMn_6Sn_6 , at zero temperature, the FM component dominates, and the ground state is the same as in TbMn_6Sn_6 . However, at higher temperatures, the Er moment starts to fluctuate (much more so than Mn, as shown in Ref. (14)), so the indirect exchange coupling $J_{\text{R-Mn}}$ is reduced compared to the direct coupling J_2 , and eventually, the system switches to a spiral state, similar to YMn_6Sn_6 . With increasing field, this helical spiral transitions to a flopped

TCS state, as suggested by our neutron diffraction data (the intermediate regime in Fig. 1H highlighted by white color). Note that, unlike TbMn_6Sn_6 , ErMn_6Sn_6 is, both experimentally and computationally (4), easy-plane, so no spin-reorientation transition happens in the Er system, unlike the Tb system (14).

Discussion

By mapping the temperature and field dependence of the THE in ErMn_6Sn_6 (Fig. 2D), we reveal two characteristics that point toward a fluctuating order as the underlying mechanism of the THE. First, the THE is observed only at the boundary between the spiral and ferrimagnetic phases. Second, its magnitude increases with increasing temperature as expected from Eq. 1. In the supplementary materials, we use Eq. 1 to extract the THE signal and reproduce the phase diagram of Fig. 2C (Figs. S8 and S9), confirming its connection with Mn spin fluctuations.

The field dependence of the magnetic satellite peak intensities in Figs. 1F,H show that an intermediate fluctuating magnetic phase (TCS) exists between the spiral and ferrimagnetic phases. The THE emerges from the fluctuations of Mn spins in this phase. Interestingly, the underlying spiral AFM state, the dome in Fig. 1D, is in and of itself a result of fluctuations, but this time Er instead of Mn. A prerequisite for that is reduced Er-Mn coupling, compared to Tb-Mn. As seen in Fig. 3, the Tb-f bands are too close to E_F in TbMn_6Sn_6 unlike the Er-f bands in ErMn_6Sn_6 , confirming the above picture. Thus, both the nontrivial magnetic phase diagram and the THE are driven by spin fluctuations, albeit of Er moments in the former, and Mn moments in the latter.

Materials and Methods

Material Synthesis.

Single crystals of ErMn_6Sn_6 were grown using a self-flux technique. Erbium pieces (99.9%), manganese granules (99.98%), and tin pieces (99.999%) were mixed with the ratio Er:Mn:Sn =

1.25:6:18 and placed in an alumina crucible inside an evacuated quartz tube. The excess amount (25%) of rare-earth was necessary to eliminate impurity phases such as Mn_3Sn_2 and ErMnSn_2 . The quartz tube was heated in a box furnace to 1000°C at $3^\circ\text{C}/\text{min}$, held at that temperature for 12h, cooled to 600°C at $6^\circ\text{C}/\text{h}$, and centrifuged to remove the excess flux. Using less amounts of rare-earth or centrifuging at $T < 600^\circ\text{C}$ resulted in the formation of impurity phases.

Characterizations.

Powder x-ray diffraction (PXRD) was performed using a Bruker D8 ECO instrument in the Bragg-Brentano geometry, using a copper source (Cu-K_α) and a LYNXEYE XE 1D energy dispersive detector. The FullProf suite was used for the Rietveld analysis (28) and the VESTA program was used for crystal visualizations (29). Magnetization was measured using a Quantum Design MPMS3 with the sample mounted on a low-background quartz holder. The electrical resistivity and Hall effect were measured in a four-probe configuration using a Quantum Design PPMS Dynacool.

First-Principles Calculations

The magnetic and electronic structures of $(\text{Y,Er,Tb})\text{Mn}_6\text{Sn}_6$ we calculated from first-principle by including spin-orbit coupling within the framework of density functional theory (DFT) (30) using the Vienna *ab-initio* simulation package (VASP) (31, 32). The ground state electronic structure was obtained with the projector augmented-wave pseudopotential, while the electron exchange-correlation effects were implemented by the generalized gradient approximation (GGA) (33) with Perdew-Burke-Ernzerhof (PBE) parametrization. The energy cut-off of 350 eV was used for the plane-wave basis set, and the Brillouin zone (BZ) integration was performed with a $9 \times 9 \times 7$ Γ -centered k -mesh (34). The total energy tolerance criteria are set to 10^{-8} eV to satisfy self-consistency. We utilized experimental structure parameters and optimized ionic positions until the residual forces on each ion were less than 10^{-2} eV/Å and the stress tensors became negligible.

In our calculations, we considered the inadequacy of DFT methods in respecting the 2nd and 3rd Hund's rules (4). The problem is that these methods include spurious self-interaction of f-orbitals, which, because of their strong localization, is larger than the spin-orbit and crystal field effects. As a result, the occupation state of the f-shell becomes unstable and deviates from the Hund's rules depending on the magnetic structure. To circumvent this problem, we used a patch to the VASP (31, 32) code, which allows nudging DFT+U calculations into a given orbital configuration (35).

Neutron Single Crystal Diffraction.

Zero-field neutron diffraction data for ErMn_6Sn_6 (Sample 1) were collected on the time-of-flight single crystal diffractometer, TOPAZ, at the Spallation Neutron Source, Oak Ridge National Laboratory (36). A plate-shaped crystal measuring 0.49 x 3.16 x 3.25 mm was securely attached to a custom-built aluminum pin with SuperGlue and then mounted on the TOPAZ ambient goniometer for data collection at 200 K, with its temperature controlled by an LN2 Cobra Cryostream. Data collection at 5 K used the TOPAZ cryogenic goniometer, with sample temperature controlled by a Cryomech P415 pulse tube cryocooler. Crystal orientations were optimized with the CrystalPlan program (37) (19 at 200 K and 20 at 5 K). Measurement for each orientation used approximately 1 hour of neutron beamtime, with 5 Coulombs of proton charge for SNS beam power at 1.4 MW. A multiresolution machine learning algorithm was used for peak integration. Data normalization, including neutron time-of-flight spectrum, Lorentz, and detector efficiency corrections, followed previously reported procedures (38). A spherical absorption correction with $\mu = 0.02155 + 0.05705\lambda \text{ mm}^{-1}$ was applied. The reduced data were saved in SHELX HKLF2 format, with the wavelength for each reflection recorded separately and not merged. Magnetic structure solution and refinement were performed using the JANA2020 program (39). The crystal structures at 200 K and 40 K from X-ray diffraction, both of $P6/mmm$ parent space group symmetry, served as the starting models for magnetic structure refinements.

Neutron diffraction data under a magnetic field were measured on the thermal-neutron single crystal diffractometer ZEBRA at SINQ of Paul Scherrer Institut (Villigen, Switzerland). The instrument was operated in the normal beam geometry. An incoming neutron wavelength of 1.383 Å (Ge monochromator) was used. A crystal of dimensions 3.25 mm × 2.83 mm × 1 mm was mounted in vertical 6 T or horizontal 7 T magnets with the b^* crystal axis vertical. In addition to temperature and magnetic field scans, data sets in magnetic fields applied vertically were collected. 28 and 23 magnetic reflections were measured at $T = 200$ K and $H = 1.5$ T and $H = 3.5$ T, respectively, and were used for refinements of magnetic models using FULLPROF and JANA.

References

1. M. Norman, Colloquium: Herbertsmithite and the search for the quantum spin liquid. *Reviews of Modern Physics* **88**, 041002 (2016).
2. N. J. Ghimire, I. I. Mazin, Topology and correlations on the kagome lattice. *Nature Materials* **19**, 137-138 (2020).
3. E. Tang, J.-W. Mei, X.-G. Wen, High-Temperature Fractional Quantum Hall States. *Physical Review Letters* **106**, 236802 (2011).
4. Y. Lee, R. Skomski, X. Wang, P. P. Orth, Y. Ren, B. Kang, A. K. Pathak, A. Kutepov, B. N. Harmon, R. J. McQueeney, I. I. Mazin, L. Ke, Interplay between magnetism and band topology in Kagome magnets RMn_6Sn_6 . *Physical Review B* **108**, 045132 (2023).
5. I. I. Mazin, H. O. Jeschke, F. Lechermann, H. Lee, M. Fink, R. Thomale, R. Valentí, Theoretical prediction of a strongly correlated Dirac metal. *Nature Communications* **5**, 4261 (2014).
6. A. Bolens, N. Nagaosa, Topological states on the breathing kagome lattice. *Physical Review B* **99**, 165141 (2019).

7. M. Kang, L. Ye, S. Fang, J.-S. You, A. Levitan, M. Han, J. I. Facio, C. Jozwiak, A. Bostwick, E. Rotenberg, M. K. Chan, R. D. McDonald, D. Graf, K. Kaznatcheev, E. Vescovo, D. C. Bell, E. Kaxiras, J. van den Brink, M. Richter, M. Prasad Ghimire, J. G. Checkelsky, R. Comin, Dirac fermions and flat bands in the ideal kagome metal FeSn. *Nature Materials* **19**, 163–169 (2020).
8. G. Venturini, B. C. E. Idrissi, B. Malaman, Magnetic properties of RMn_6Sn_6 (R = Sc, Y, Gd-Tm, Lu) compounds with HfFe_6Ge_6 type structure. *Journal of Magnetism and Magnetic Materials* **94**, 35–42 (1991).
9. B. C. El Idrissi, G. Venturini, B. Malaman, D. Fruchart, Magnetic structures of TbMn_6Sn_6 and HoMn_6Sn_6 compounds from neutron diffraction study. *Journal of the Less Common Metals* **175**, 143–154 (1991).
10. D. I. Gorbunov, M. D. Kuz'min, K. Uhlířová, M. Žáček, M. Richter, Y. Skourski, A. V. Andreev, Magnetic properties of a GdMn_6Sn_6 single crystal. *Journal of Alloys and Compounds* **519**, 47–54 (2012).
11. X. Xu, J.-X. Yin, W. Ma, H.-J. Tien, X.-B. Qiang, P. V. S. Reddy, H. Zhou, J. Shen, H.-Z. Lu, T.-R. Chang, Z. Qu, S. Jia, Topological charge-entropy scaling in kagome Chern magnet TbMn_6Sn_6 . *Nature Communications* **13**, 1197 (2022).
12. S. Riberolles, T. J. Slade, D. Abernathy, G. Granroth, B. Li, Y. Lee, P. Canfield, B. Ueland, L. Ke, R. McQueeney, Low-Temperature Competing Magnetic Energy Scales in the Topological Ferrimagnet TbMn_6Sn_6 . *Physical Review X* **12**, 021043 (2022).
13. C. Mielke III, W. L. Ma, V. Pomjakushin, O. Zaharko, S. Sturniolo, X. Liu, V. Ukleev, J. S. White, J.-X. Yin, S. S. Tsirkin, C. B. Larsen, T. A. Cochran, M. Medarde, V. Porée, D. Das, R. Gupta, C. N. Wang, J. Chang, Z. Q. Wang, R. Khasanov, T. Neupert, A. Amato, L. Liborio, S. Jia, M. Z. Hasan, H. Luetkens, Z. Guguchia, Low-temperature magnetic

- crossover in the topological kagome magnet TbMn_6Sn_6 . *Communications Physics* **5**, 1–9 (2022).
14. D. C. Jones, S. Das, H. Bhandari, X. Liu, P. Siegfried, M. P. Ghimire, S. S. Tsirkin, I. I. Mazin, N. J. Ghimire, Origin of spin reorientation and intrinsic anomalous Hall effect in the kagome ferrimagnet TbMn_6Sn_6 (2022). ArXiv:2203.17246 [cond-mat].
 15. R. L. Dally, J. W. Lynn, N. J. Ghimire, D. Michel, P. Siegfried, I. I. Mazin, Chiral properties of the zero-field spiral state and field-induced magnetic phases of the itinerant kagome metal YMn_6Sn_6 . *Physical Review B* **103**, 094413 (2021).
 16. N. J. Ghimire, R. L. Dally, L. Poudel, D. C. Jones, D. Michel, N. T. Magar, M. Bleuel, M. A. McGuire, J. S. Jiang, J. F. Mitchell, J. W. Lynn, I. I. Mazin, Competing magnetic phases and fluctuation-driven scalar spin chirality in the kagome metal YMn_6Sn_6 . *Science Advances* **6**, eabe2680 (2020).
 17. H. Zhang, C. Liu, Y. Zhang, Z. Hou, X. Fu, X. Zhang, X. Gao, J. Liu, Magnetic field-induced nontrivial spin chirality and large topological Hall effect in kagome magnet ScMn_6Sn_6 . *Applied Physics Letters* **121**, 202401 (2022).
 18. J. Casey, S. S. Samatham, C. Burgio, N. Kramer, A. Sawon, J. H. and, A. K. Pathak, Spin-flop quasi metamagnetic, anisotropic magnetic, and electrical transport behavior of Ho substituted kagome magnet ErMn_6Sn_6 (2023).
 19. B. Malaman, G. Venturini, R. Welter, J. P. Sanchez, P. Vulliet, E. Ressouche, Magnetic properties of RMn_6Sn_6 (R=Gd–Er) compounds from neutron diffraction and Mössbauer measurements. *Journal of Magnetism and Magnetic Materials* **202**, 519–534 (1999).
 20. T. Kurumaji, T. Nakajima, M. Hirschberger, A. Kikkawa, Y. Yamasaki, H. Sagayama, H. Nakao, Y. Taguchi, T.-h. Arima, Y. Tokura, Skyrmion lattice with a giant topological Hall effect in a frustrated triangular-lattice magnet. *Science* **365**, 914–918 (2019).

21. Q. Shao, Y. Liu, G. Yu, S. K. Kim, X. Che, C. Tang, Q. L. He, Y. Tserkovnyak, J. Shi, K. L. Wang, Topological Hall effect at above room temperature in heterostructures composed of a magnetic insulator and a heavy metal. *Nature Electronics* **2**, 182–186 (2019).
22. N. Verma, Z. Addison, M. Randeria, Unified theory of the anomalous and topological Hall effects with phase-space Berry curvatures. *Science Advances* **8**, eabq2765 (2022).
23. Q. Wang, K. J. Neubauer, C. Duan, Q. Yin, S. Fujitsu, H. Hosono, F. Ye, R. Zhang, S. Chi, K. Krycka, H. Lei, P. Dai, Field-induced topological Hall effect and double-fan spin structure with a c -axis component in the metallic kagome antiferromagnetic compound YMn_6Sn_6 . *Physical Review B* **103**, 014416 (2021).
24. M. Afshar, I. I. Mazin, Spin spiral and topological hall effect in Fe_3Ga_4 . *Phys. Rev. B* **104**, 094418 (2021).
25. V. I. Anisimov, J. Zaanen, O. K. Andersen, Band theory and mott insulators: Hubbard U instead of stoner I. *Phys. Rev. B* **44**, 943 (1991).
26. V. I. Anisimov, F. Aryasetiawan, A. I. Lichtenstein, First-principles calculations of the electronic structure and spectra of strongly correlated systems: the LDA + U method. *Journal of Physics: Condensed Matter* **9**, 767 (1997).
27. A. Galler, L. V. Pourovskii, Electronic structure of rare-earth mononitrides: quasiautomic excitations and semiconducting bands. *New Journal of Physics* **24**, 043039 (2022).
28. J. Rodríguez-Carvajal, Recent advances in magnetic structure determination by neutron powder diffraction. *Physica B: Condensed Matter* **192**, 55–69 (1993).
29. K. Momma, F. Izumi, VESTA 3 for three-dimensional visualization of crystal, volumetric and morphology data. *Journal of Applied Crystallography* **44**, 1272–1276 (2011).
30. P. Hohenberg, W. Kohn, Inhomogeneous electron gas. *Physical review* **136**, B864 (1964).

31. G. Kresse, J. Furthmüller, Efficient iterative schemes for ab initio total-energy calculations using a plane-wave basis set. *Physical review B* **54**, 11169 (1996).
32. G. Kresse, D. Joubert, From ultrasoft pseudopotentials to the projector augmented-wave method. *Physical review b* **59**, 1758 (1999).
33. J. P. Perdew, K. Burke, M. Ernzerhof, Generalized gradient approximation made simple. *Physical review letters* **77**, 3865 (1996).
34. H. J. Monkhorst, J. D. Pack, Special points for brillouin-zone integrations. *Phys. Rev. B* **13**, 5188 (1976).
35. J. P. Allen, G. W. Watson, Occupation matrix control of d- and f-electron localisations using dft + u. *Phys. Chem. Chem. Phys.* **16**, 21016-21031 (2014).
36. L. Coates, H. B. Cao, B. C. Chakoumakos, M. D. Frontzek, C. Hoffmann, A. Y. Kovalevsky, Y. Liu, F. Meilleur, A. M. dos Santos, D. A. A. Myles, X. P. Wang, F. Ye, A suite-level review of the neutron single-crystal diffraction instruments at Oak Ridge National Laboratory. *Review of Scientific Instruments* **89**, 092802 (2018).
37. J. Zikovsky, P. F. Peterson, X. P. Wang, M. Frost, C. Hoffmann, CrystalPlan: an experiment-planning tool for crystallography. *Journal of Applied Crystallography* **44**, 418–423 (2011). Publisher: International Union of Crystallography.
38. A. J. Schultz, M. R. V. Jørgensen, X. Wang, R. L. Mikkelsen, D. J. Mikkelsen, V. E. Lynch, P. F. Peterson, M. L. Green, C. M. Hoffmann, Integration of neutron time-of-flight single-crystal Bragg peaks in reciprocal space. *Journal of Applied Crystallography* **47**, 915–921 (2014). Publisher: International Union of Crystallography.
39. V. Petříček, L. Palatinus, J. Plášil, M. Dušek, Jana2020 – a new version of the crystallographic computing system jana. *Zeitschrift für Kristallographie - Crystalline Materials* **238**, 271–282 (2023).

Acknowledgements: The authors thank M. Newburger and M. Page for insightful discussions, and O. Remcho, X. Yao, and T. Hogan for assistance with the experiments. The work at Boston College was supported by the National Science Foundation under Award No. DMR-2203512. The work at Howard University was supported by the U.S. Department of Energy (DOE), Office of Science, Basic Energy Sciences under Award No. DE-SC0022216. This research at Howard University used resources of the National Energy Research Scientific Computing Center, a DOE Office of Science User Facility supported by the Office of Science of the U.S. Department of Energy under Contract No. DE-AC02-05CH11231 using NERSC award BES-ERCAP0023852 and Accelerate ACCESS PHY220127. Our neutron scattering experiments were performed at the Swiss Spallation Neutron Source SINQ, Paul Scherrer Institut, Switzerland, and the Spallation Neutron Source, a DOE Office of Science User Facility operated by the Oak Ridge National Laboratory, USA. P.B. thanks SNSF projects 200021-188707 and 200020-182536 for financial support. Certain commercial products or company names are identified here to describe our study adequately. Such identification is not intended to imply recommendation or endorsement by the National Institute of Standards and Technology, nor is it intended to imply that the products or names identified are necessarily the best available for the purpose.

Author Contributions: K.W.F. grew the crystals and performed magnetization and transport characterizations. A.S., X.W., P.B., O.Z., and W.D.R. performed neutron diffraction experiments. S.M. and S.C. calculated the band structure and electronic properties. W.D.R., I.I.M. and F.T. conceptualized and organized the project. All authors participated in the discussions and in writing the paper.

Competing Interests: The authors declare no competing interests.

Data and materials availability: Additional data and materials are available online.

Supplementary Material: Supplementary materials include a PDF file and two mCIF files.

Supplementary Materials

Topological Hall effect induced by chiral fluctuations in a kagome lattice

Kyle W. Fruhling^{1*}, Alenna Streeter^{1*}, Sougata Mardanya²,
Xiaoping Wang³, Priya Baral⁴, Oksana Zaharko⁴,
Igor I. Mazin⁵, Sugata Chowdhury², William D. Ratcliff^{6,7}, Fazel Tafti^{1*}

¹Department of Physics, Boston College, Chestnut Hill, MA 02467, USA

²Department of Physics and Astrophysics, Howard University, Washington, DC 20059, USA

³Neutron Scattering Division, Oak Ridge National Laboratory, Oak Ridge, TN 37831, USA

⁴Laboratory for Neutron Scattering and Imaging (LNS), Paul Scherrer Institut, PSI,
Villigen, CH-5232, Switzerland

⁵Department of Physics and Astronomy and Quantum Science and Engineering Center,
George Mason University, Fairfax, VA 22030, USA

⁶NIST Center for Neutron Research, National Institute of Standards and Technology,
Gaithersburg, ME 20899-6100, USA

⁷Department of Physics and Department of Materials Science and Engineering,
University of Maryland, College Park, Maryland 20742, USA

*fazel.tafti@bc.edu

This PDF file includes supplementary text, Figures S1 to S9, and Tables S1 to S4.

*These authors contributed equally to this work.

Magnetization Data

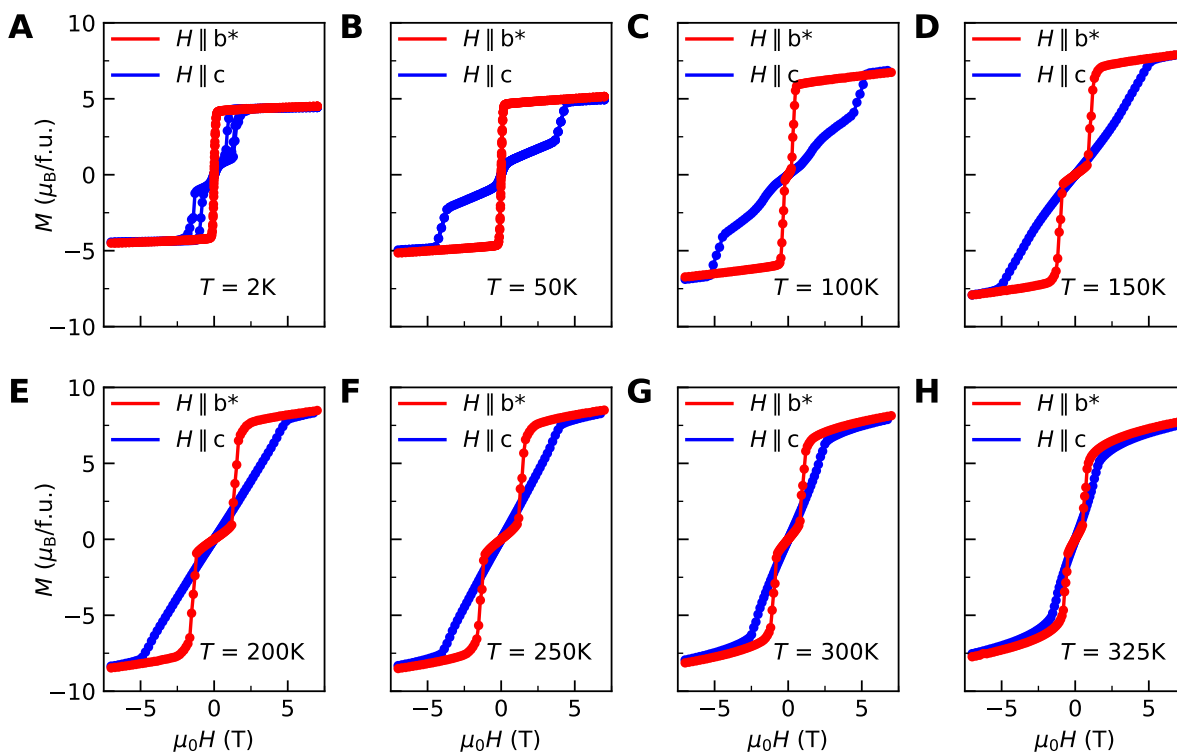


Figure S1: **Magnetization curves.** (A-H) Magnetization curves in both field directions $H||b^*$ (red) and $H||c$ (blue) are shown at several temperatures.

Figure S1 shows magnetization curves at different temperatures for both $H||b^*$ (red) and $H||c$ (blue) from which we constructed the phase diagrams in Fig. S2. At low temperatures with $H||c$, there is notable hysteresis. At these low temperatures, the critical field is defined as the average of the critical field with field increasing and of the critical field with field decreasing. Our discussion in the main text was focused on the phase diagram for $H||b^*$ shown in Fig. S2B and reproduced in the main text (Fig. 1F).

Neutron Diffraction Data from the Zebra Experiment

Here we show the complete set of neutron diffraction data used to construct the phase diagrams with $H||b^*$ and $H||c$. Figures S3A and S3B show the (002) reflection and magnetic satellite

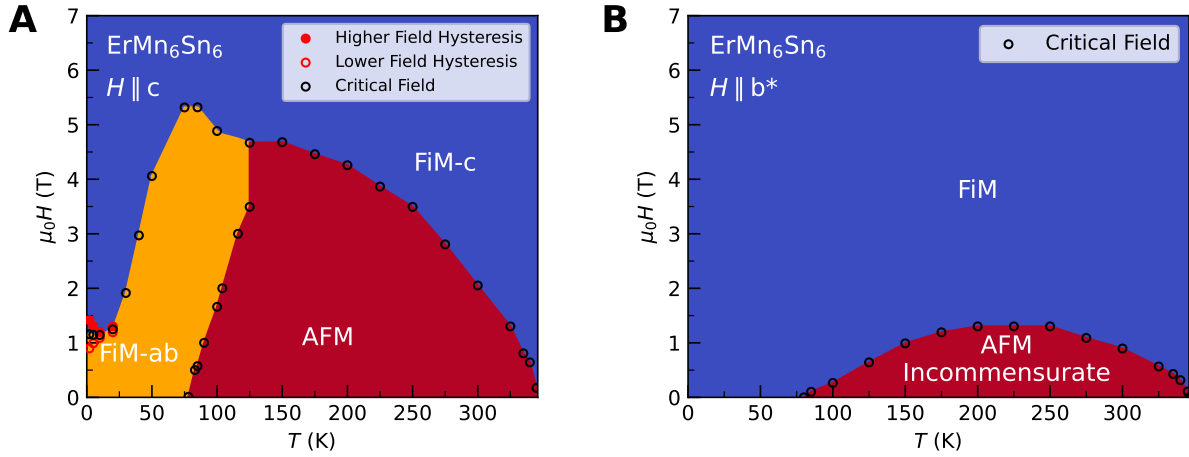


Figure S2: **Magnetic phase diagrams.** (A) Magnetic phase diagram with $H \parallel c$. (B) Magnetic phase diagram with $H \parallel b^*$.

peaks at $T = 325$ K with magnetic fields along the b^* and c axis directions, respectively. Note that only one of the satellites, i.e. the one at $(0, 0, L - \mathbf{k})$, is shown, because measuring both satellites was too time consuming within the beamtime period we had for measurements. In both directions, increasing the magnetic field suppresses the satellite peaks. This suppression is completed at 1 T for $H \parallel b^*$ and 2 T for $H \parallel c$. Each peak is fit with a Gaussian peak shape. Similar data are shown in Figures S3C ($H \parallel b^*$) and S3D ($H \parallel c$) at $T = 300$ K.

Panels E and F show the integrated intensity of the incommensurate magnetic peaks (satellite peaks) at $T = 325$ K in panels A and B as a function of field strength. These satellite peaks are observed at $\mathbf{Q} = (0, 0, 1.781)$ and $\mathbf{Q} = (0, 0, 1.783)$ as stated on Figures S3E and S3F. For $H \parallel b^*$ (Fig. S3E), the suppression takes on a sigmoidal shape with a sharp decrease in intensity before 1 T. For $H \parallel c$ (Fig. S3F), a more gradual power law behavior is observed with complete suppression at 2 T. Similar behaviors are observed at $T = 300$ K in Figures S3G and S3H, with a sigmoidal suppression of the satellite peaks for $H \parallel b^*$ and a power-law suppression for $H \parallel c$.

Panels I and J show the integrated intensity of the (002) nuclear peak as a function of field strength at $T = 325$ K. For $H \parallel b^*$ (Figure S3I), the nuclear intensity remains relatively unchanged in field. We also note that Crystal #2 shows a small intensity peak at the critical field, a feature which does not occur in Crystal #1. For $H \parallel c$ (Figure S3J), the nuclear inten-

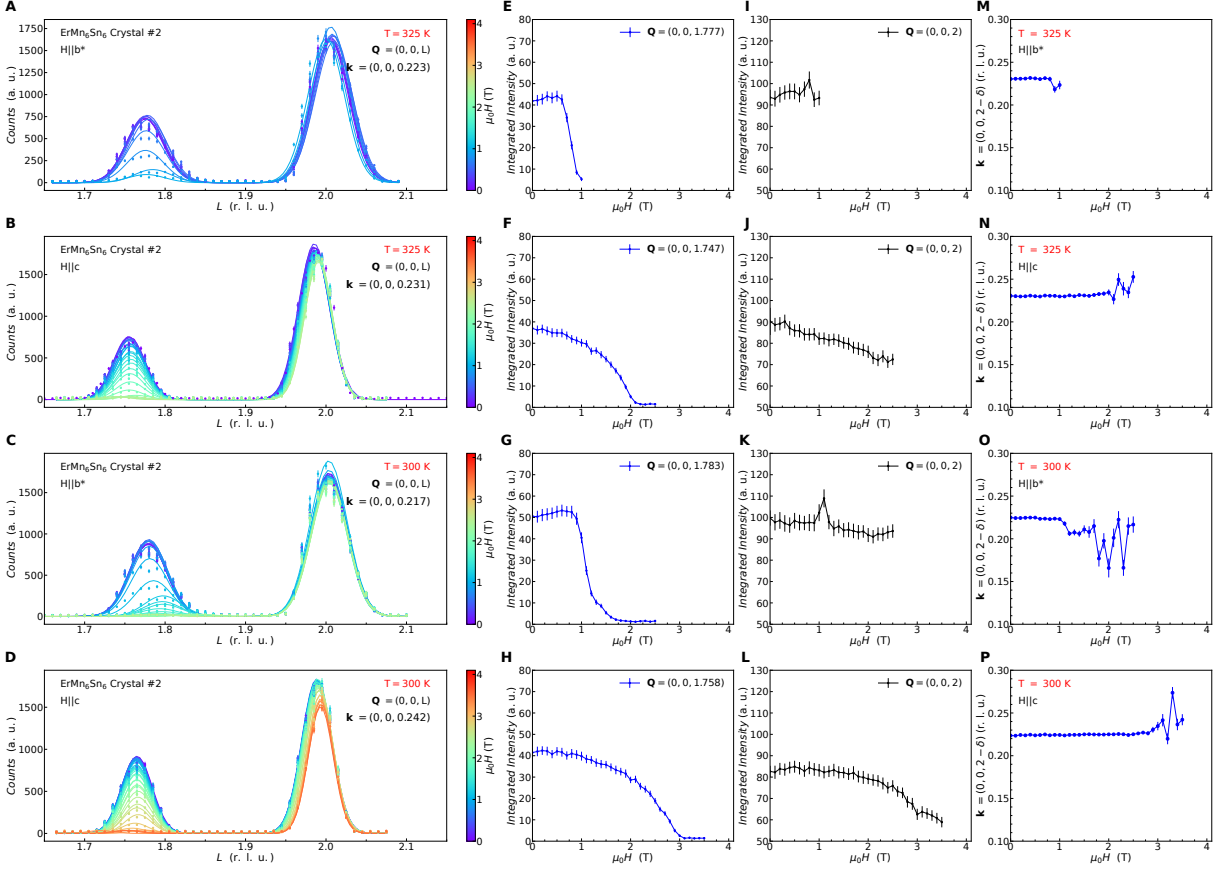


Figure S3: **Neutron diffraction data at 325 and 300 K.** (A-D) Q-scans obtained around the (002) reflection to reveal the magnetic satellite peak at 325 and 300 K with $H \parallel b^*$ and $H \parallel c$ as indicated on each panel. Different colors show different field strengths. (E-H) Integrated intensity of the satellite peak as a function of field strength corresponding to panels A-D, respectively. (I-L) Integrated intensity of the (002) peak as a function of field strength corresponding to panels A-D, respectively. (M-P) Incommensurate propagation wavevector as a function of field strength for panels A-D, respectively.

sity decreases gradually with increasing field. This may be an indication that there is magnetic intensity on the nuclear peaks from an additional $k = (0, 0, 0)$ order at zero-field, which is redistributed to in-plane reflections when the magnetic field polarizes spins out of plane towards the c -axis. Similar observations are made at $T = 300$ K in Figures S3K and S3L.

The magnetic propagation vector is given by the difference δ between the two peak positions and is displayed as a function of field at $T = 325$ K in panels M and N. For $H \parallel b^*$ (Figure S3M), there is a subtle shift in the satellite peak position at the transition field, illustrated by the dip in δ . The shift, which is more noticeable at lower temperatures, indicates an intermediate magnetic

phase between the AFM and FIM orders in the phase diagram of Fig. S2B. There is no shift in the propagation vector for $H\parallel c$ (Figure S3N).

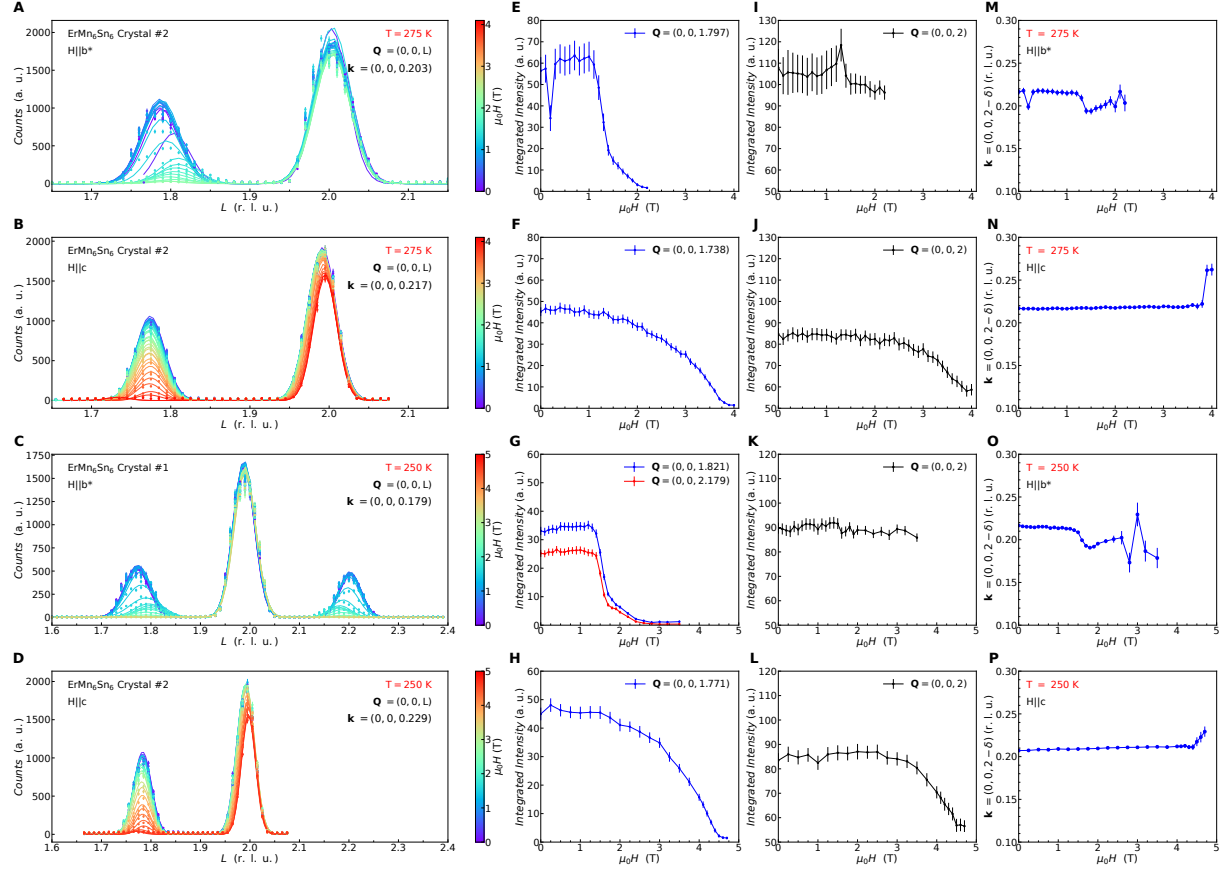


Figure S4: **Neutron diffraction data at 275 and 250 K.** (A-D) Q-scans obtained around the (002) reflection to reveal the magnetic satellite peak at 275 and 250 K with $H\parallel b^*$ and $H\parallel c$ as indicated on each panel. Different colors show different field strengths. (E-H) Integrated intensity of the satellite peak as a function of field strength corresponding to panels A-D, respectively. (I-L) Integrated intensity of the (002) peak as a function of field strength corresponding to panels A-D, respectively. (M-P) Incommensurate propagation wavevector as a function of field strength for panels A-D, respectively.

The same features at 325 and 300 K are also present at 275 and 250 K as shown in Fig. S4. Several systematic trends in Figs. S3 and S4 can be summarized as follows. (i) The scans shown in Figs. S3A-D and S4A-D include both the (0,0,2) nuclear Bragg peak and a smaller satellite peak at an incommensurate $Q = (0, 0, 2 - \delta)$. This general structure is best observed in Fig. S4C with the nuclear (0,0,2) peak at the center and two satellite peaks on either side of it. That scan was obtained for Crystal #1 at 250 K and with $H\parallel b^*$. Due to experimental time

constraint, we only measured the satellite peak at the smaller Q -vector at all other temperatures and field directions. (ii) The suppression of the satellite peak intensity with field always follows a sigmoidal behavior for $H\parallel b^*$ (Panels E and G) and a power law behavior for $H\parallel c$ (Panels F and H). (iii) The nuclear (0,0,2) peak does not show any field dependence when $H\parallel b^*$ (Panels I and K), but it shows a mild suppression when $H\parallel c$ (Panels J and L). From here, we conclude that the magnetic structure is in-plane for $H\parallel b^*$, but when $H\parallel c$ the spins are canting out of plane and the magnetic structure acquires a FM component.

Neutron Diffraction Data from the TOPAZ Experiment

We used the TOPAZ single-crystal diffractometer to refine the magnetic structure of ErMn_6Sn_6 in both FIM and AFM phases (see the phase diagram of Fig. S2B) in zero-field. Prior to the refinement analysis of neutron data, we determined the crystal structure at 40 K and 200 K from X-ray diffraction, and found it to be in the $P6/mmm$ space group symmetry at both low and high temperatures. We used this structural model as the starting point for the magnetic refinements of neutron single crystal diffraction data measured at 5 K and 200 K in Tables S1 and S3.

First, we discuss the magnetic structure at 5 K, i.e. the magnetic ground state of ErMn_6Sn_6 . As listed in Table S1, we found fits of the data in two magnetic space groups, namely a $C2'/m'$ space group and a $Cmm'm'$. Since the latter has a higher symmetry than the former, we identify $Cmm'm'$ as the magnetic ground state of the material. Individual components of the magnetic moment for different Er and Mn sites are listed in Table S2 for this structure, which is referred to as the FIM order in the main manuscript. Figure S5 illustrates the FIM arrangement of magnetic moments at 5 K.

Next, we discuss the magnetic structure at 200 K. We found two magnetic models that could fit the neutron diffraction data at 200 K (Table S3). The first model in the magnetic space groups $P622.1(00g)h00s$ has a spiral AFM order as shown in Fig. S6. Individual components

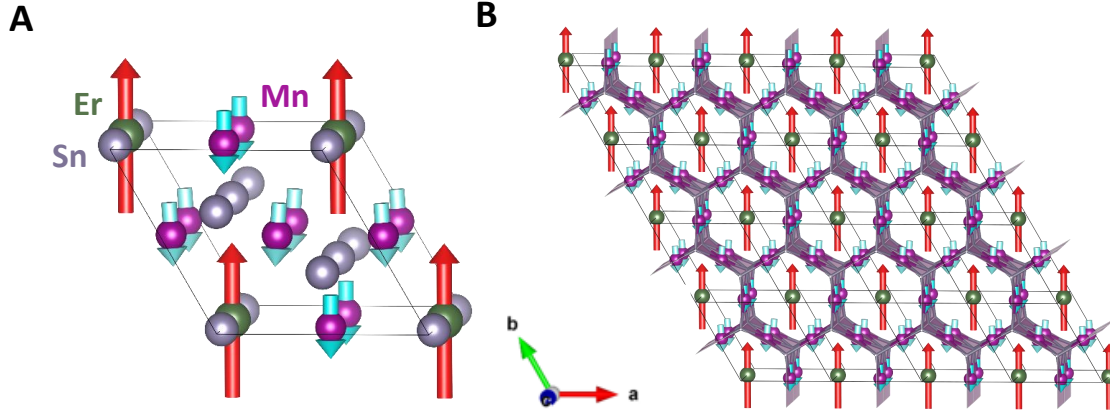


Figure S5: **Magnetic structure of ErMn_6Sn_6 at 5K and zero-field.** (a) Ferrimagnetic structure with all atoms in the space group $Cmm'm'$; (b) Ferrimagnetic structure with Sn atoms omitted for clarity. The Mn moments in the Kagome lattice comprising $(\text{Mn}_3\text{Sn}_2)_2$ subunits interact antiferromagnetically with Er atoms in the channels.

of the magnetic moment for different Er and Mn sites are listed in Table S4 for this structure, which is referred to as the spiral AFM order in the main manuscript. The second model in the magnetic space group $Cmmm.1'(00g)s00s$ also has a spiral for the Mn moments. However, the Er moments have a collinear arrangement of spins with an amplitude-modulated moments. We rule out this magnetic structure based on two reasons: first, it implies that the Mn and Er sublattices are independent from each other which contradicts the DFT results; second, this is a lower symmetry solution compared to the double-spiral structure. As such, we only show the double spiral AFM order associated with $P622.1'(00g)h00s$ in the main manuscript.

Topological Hall Effect (THE)

The color scale in Fig. 2G of the main text represents the magnitude of the THE (ρ^T) determined by the analysis shown in Fig. S7. At each temperature, we extract THE by subtracting the anomalous and ordinary contributions from the total Hall effect, as explained in the main text. To create the color map, this analysis was carried out at several temperatures, and then a linear interpolation was applied between THE magnitudes extracted at different temperatures.

Table S1: Crystal data and magnetic structure refinement details for ErMn₆Sn₆ at 5 K and zero-field.

Chemical formula	ErMn ₆ Sn ₆	
M_r	1209.1	
Parent crystal system, space group	Hexagonal, $P6/mmm$	
Temperature (K)	5	
a, c (Å)	5.4934 (4), 8.9700 (9)	
V (Å ³)	234.43 (3)	
Z	1	
Propagation vector	$\mathbf{k} = (0, 0, 0)$	
Magnetic (super)space group No.	65.486	12.62
BNS Magnetic (super)space group	$Cmm'm'$	$C2'/m'$
Transformation to a standard setting	$\mathbf{a}+2\mathbf{b}, -\mathbf{a}, \mathbf{c} \mid (0,0,0)$	$-\mathbf{a}-2\mathbf{b}, \mathbf{a}, \mathbf{c} \mid (0,0,0)$
a, b, c (Å)	9.5148, 5.4934, 8.9700	
Active Irreps		
Radiation type	TOF Neutron, $\lambda = 0.5 - 3.5$ Å	
μ (mm ⁻¹)	0.02155 + 0.05705 λ	
Crystal size (mm)	3.29 × 3.16 × 0.49	
Diffractometer	SNS BL-12 TOPAZ	
Tmin, Tmax	0.625, 0.909	
No. of measured, independent, and observed [$I > 3\sigma(I)$] reflections	5814, 5814, 5693	5814, 5814, 5694
R[$F^2 > 2\sigma(F^2)$], wR(F^2), S	0.052, 0.132, 1.12	0.050, 0.125, 1.13
No. of reflections	5693	5694
No. of parameters	32	44
$\Delta\rho_{\max}, \Delta\rho_{\min}$ (f Å ⁻³)	0.36, -0.31	0.37, -0.46

Table S2: Magnetic parameters of ErMn_6Sn_6 at 5 K and zero-field, $\mathbf{k} = (0, 0, 0)$ in the space group $Cmm'm'$.

Magnetic Moments				
Atom	Mx	My	Mz	M
Er1	4.6178(2)	9.2355(3)	0.00	7.9982(4)
Mn1_1	-1.340(2)	-2.680(4)	0.00	2.321(5)
Mn1_2	-1.189(4)	-2.690(2)	0.00	2.335(5)

The sum of magnetic moments over the whole cell

Atom	Mx	My	Mz
Er1	4.6178(2)	9.2355(3)	0.00
Mn1_1	-2.680(3)	-5.360(3)	0.00
Mn1_2	-5.379(6)	-10.759(3)	0.00
Sum	-3.441(7)	-6.883(4)	0.00

The main text also discusses the expected form of the THE given by $\rho^T = \kappa M_c^2 T H$ for a transverse conical spiral (TCS) structure. Due to the complex temperature dependence of the moment, this cannot be applied directly to all temperatures with some constant κ , but can be applied at each temperature to compare the location of the peak and width of the measured THE to theory. The factor M_c^2 in the YMn_6Sn_6 case can be expressed as $1 - \frac{M^2}{M_s^2}$ where M_s is the saturation magnetization. In Fig. S8 we show the overall curve given by $\rho^T/K(T) = (1 - M^2/M_s^2)H$, where $K(T)$ is some function representing the temperature dependence, at a few different temperatures. Because this equation is only valid in the TCS phase, we do a linear interpolation between the boundary points of this region (critical fields H_1 and H_2) to determine a background which is subtracted to give the expected THE. The critical fields H_1 and H_2 are defined in Fig. S9A as follows: H_1 is the field at which a sudden increase in resistivity is observed (it is marked by a maximum in the second derivative of the resistivity as a function of field). H_2 is marked by a deviation of 10% from the high field linear fit to the $M(H)$ data. In Fig. S9B, a comparison is made between the scaled theoretical THE and measured THE to show their agreement with respect to location of the peak and width of the peak at the half maximum. Notably, the measured THE decreases slower at higher fields instead of forming a sharp peak

Table S3: Refinement details for the magnetic structure of ErMn_6Sn_6 at 200 K and zero-field.

Chemical formula	ErMn_6Sn_6	
M_r	1209.1	
Parent crystal system, space group	Hexagonal, $P6/mmm$	
Temperature (K)	200	
a, c (Å)	5.5028 (4), 8.9726 (9)	
V (Å ³)	235.30 (3)	
Z	1	
Propagation vector	$\mathbf{k} = (0, 0, 0.1959)$	
Magnetic (super)space group No.	177.1.24.2.m150.2	65.1.13.2.m482.2
BNS Magnetic (super)space group	$P622.1'(0,0,g)h00s$	$Cmmm.1'(0,0,g)s00s$
Transformation to a standard setting	$\mathbf{a}, \mathbf{b}, \mathbf{c} \mid (0,0,0,1/6)$	$\mathbf{a}, \mathbf{a}+2\mathbf{b}, \mathbf{c} \mid (0,0,0,0)$
a, b, c (Å)	5.5028, 5.5028, 8.9726	5.5028, 9.5311, 8.9726
Active Irreps		
Radiation type	Neutron, $\lambda = 0.4004 - 3.4951$ Å	
μ (mm ⁻¹)	0.02155 + 0.05705 λ	
Crystal size (mm)	3.29 × 3.16 × 0.49	
Diffractometer	SNS BL-12 TOPAZ	
Tmin, Tmax	0.624, 0.909	
No. of measured, independent, and observed [$I > 3\sigma(I)$] reflections	5527, 5527, 5233	5527, 5527, 5174
$R[F^2 > 2\sigma(F^2)]$, $wR(F^2)$, S	0.045, 0.136, 1.59	0.043, 0.122, 1.49
No. of reflections	5233	5174
No. of parameters	25	34
$\Delta\rho_{\max}, \Delta\rho_{\min}$ (e Å ⁻³)	0.23, -0.33	0.30, -0.29

Table S4: Magnetic parameters of ErMn_6Sn_6 at 200 K and zero-field, $\mathbf{k} = (0, 0, 0.1957)$ in the magnetic superspace group $P622.1'(0, 0, g)h00s$.

Magnetic moments					
Atom	wave	Mx	My	Mz	M
Er1	sin1	0.00	0.00	0.00	0.00
	cos1	2.3604(3)	4.7209(6)	0.00	4.0884(7)
Mn1	sin1	-0.2721(10)	-0.544(2)	0.00	0.471(2)
	cos1	-1.5444(10)	-3.089(2)	0.00	2.675(2)
Mn2	sin1	-0.7018(18)	-1.0566(11)	0.00	0.931(2)
	cos1	-1.1877(14)	-2.9373(11)	0.00	2.5592(18)

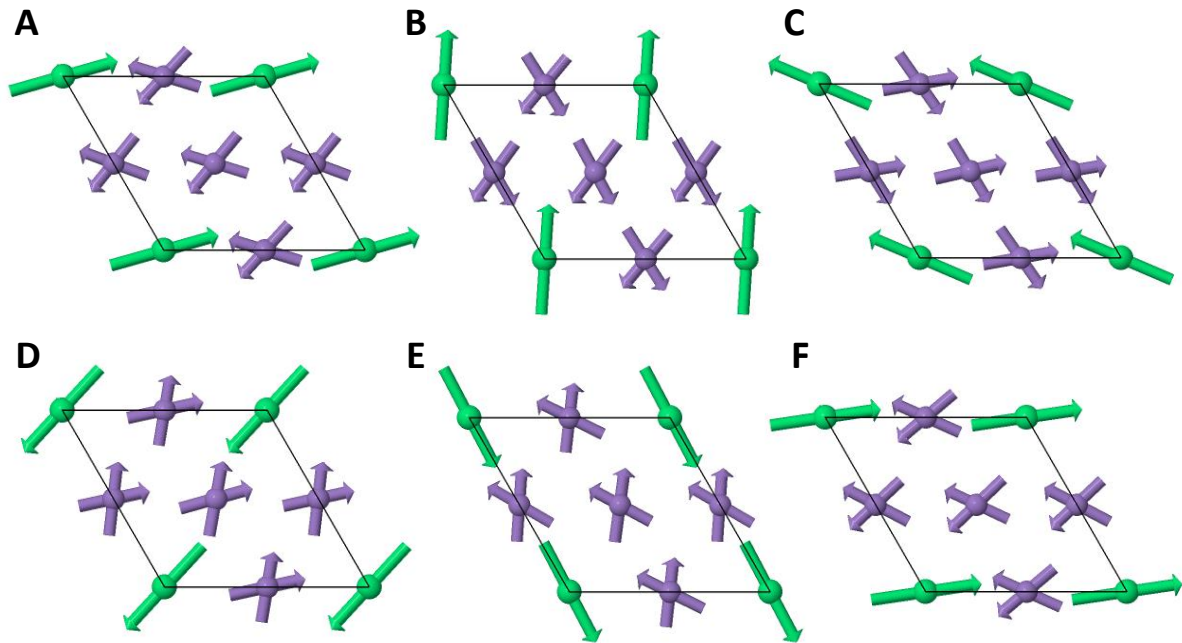


Figure S6: **Magnetic structure of ErMn_6Sn_6 at 200 K and zero field.** Magnetic structure model for ErMn_6Sn_6 solved in $P622.1'(00g)h00s$ is shown in panels (a–f), where each panel shows one Mn-Er-Mn sandwich layer. The figure shows how the spiral evolves and repeats itself after 5 Mn-Er-Mn layers.

as in the predicted THE, this is likely due to the more complicated behavior of M_c^2 due to the presence of the magnetic Er moment compared to the simpler Y case. Finally, we construct another phase diagram of the THE based on the predicted THE values which is comparable to the phase diagram constructed by direct measurement.

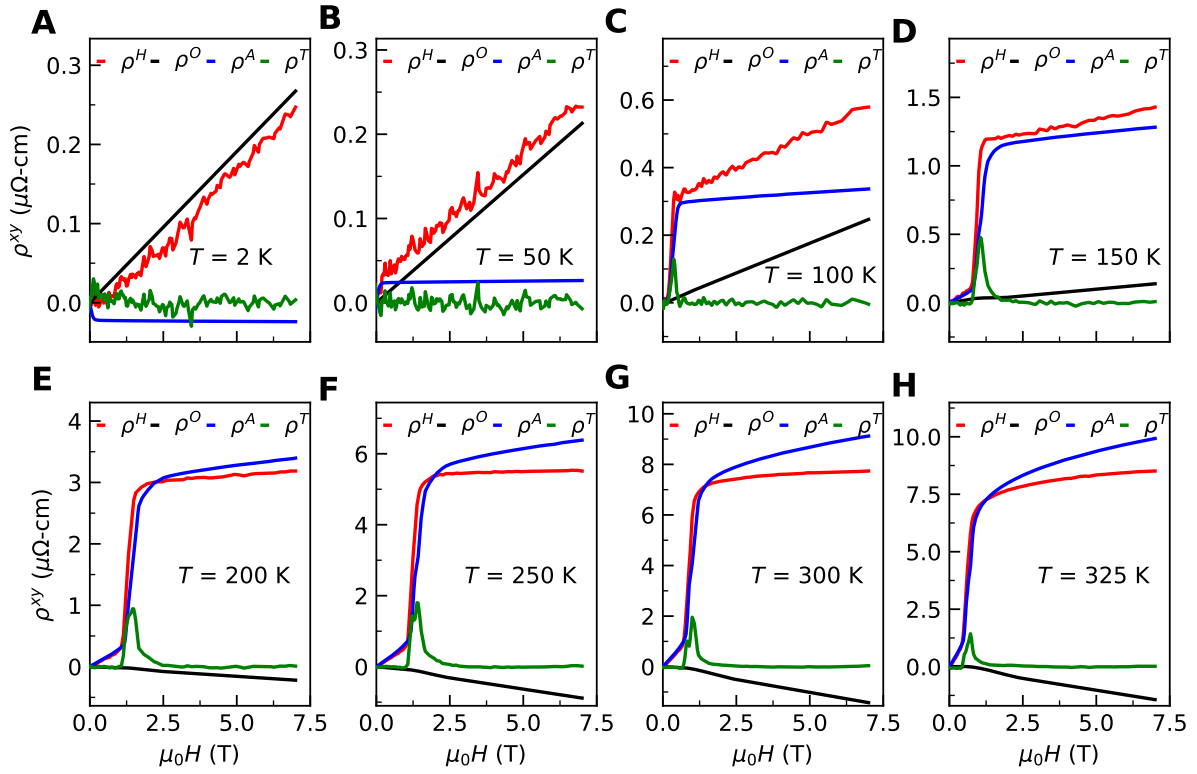


Figure S7: **Topological Hall Effect.** (A-H) The analysis of the THE at different temperatures as described in the main text.

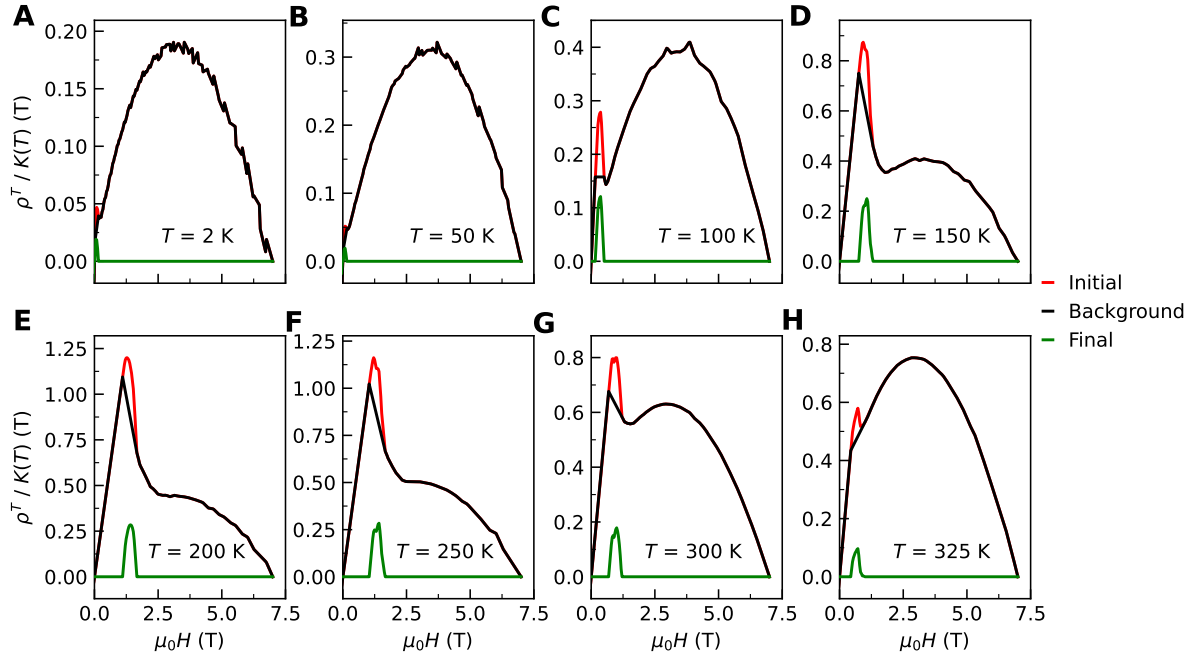


Figure S8: **Topological Hall Effect Analyzed by Theoretical Method.** (A-H) The analysis of the THE using Eq. 1 in the main text.

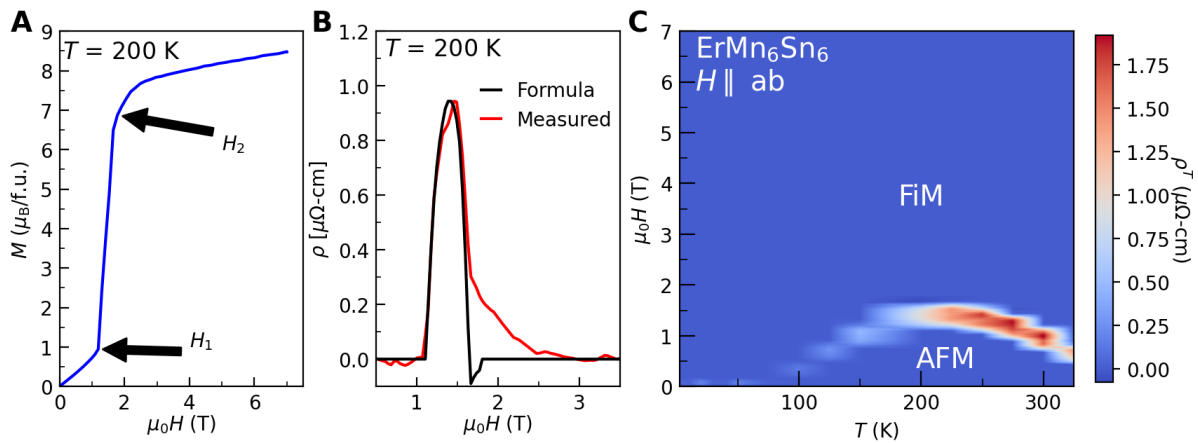


Figure S9: **Comparison of Topological Hall Analyses.** (A) Magnetization of ErMn_6Sn_6 at 200K with fields H_1 and H_2 marking the limits of the application of Eq. 1. (B) Comparison of THE extracted from resistivity data and from application of Eq. 1. (C) Phase Diagram constructed using the THE extracted using Eq. 1.